
Figures and figure supplements

Structural basis for plant plasma membrane protein dynamics and organization into functional nanodomains

Julien Gronnier *et al*

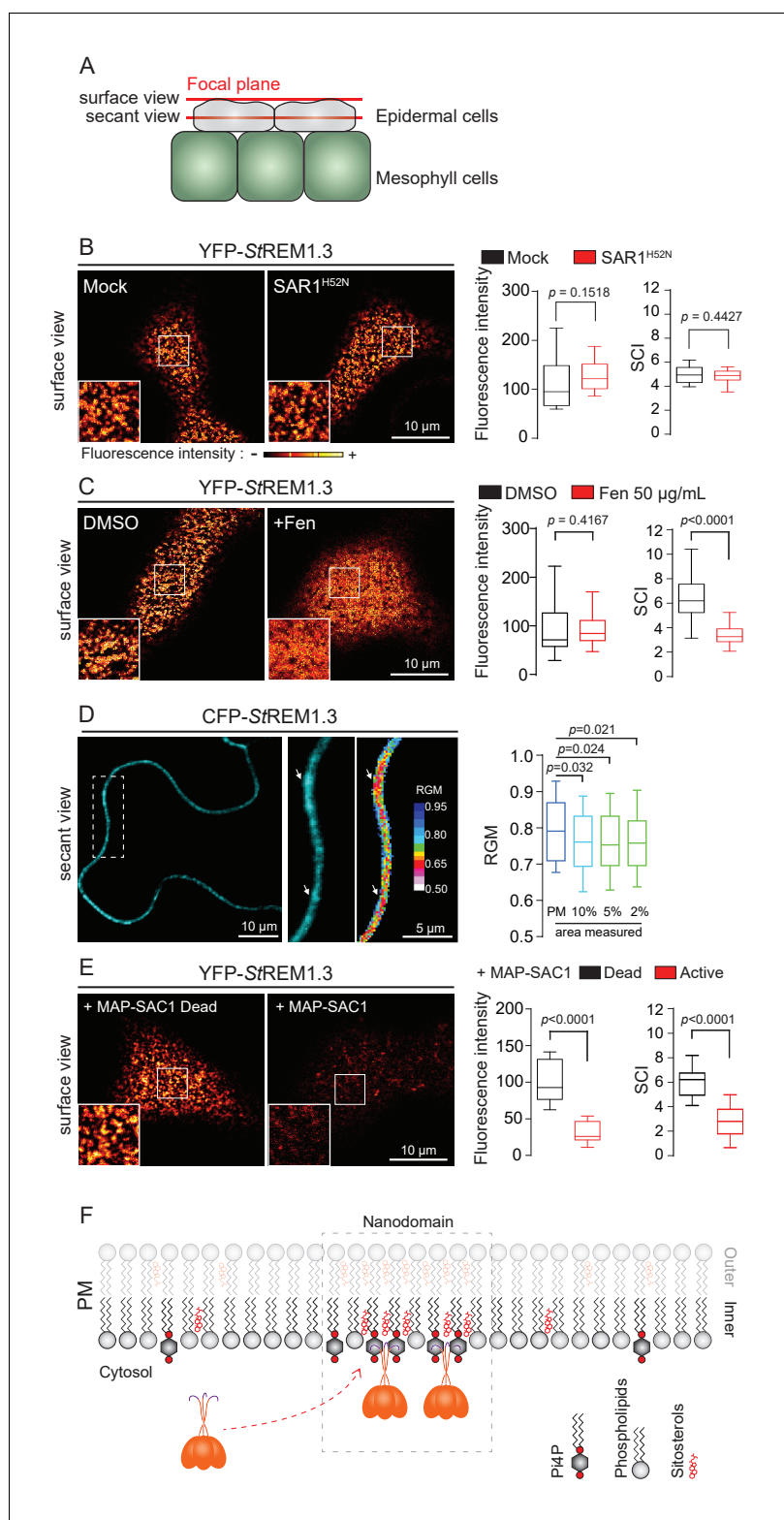


Figure 1. REMORIN localization into highly ordered PM nanodomains is mediated by sterols and PI4P. (A) Explanatory schematic of the secant or surface views of *N. benthamiana* leaf abaxial epidermal cell plasma membrane (PM) used throughout the article. (B) Confocal imaging surface views of *Nicotiana benthamiana* leaf epidermal cells expressing YFP- St REM1.3 with or without dominant-negative SAR1^{H52N} (PMA4-GFP was used as a potency control, see Figure 1—figure supplement 2), 24 hr after agroinfiltration. Tukey boxplots show the

Figure 1 continued on next page

Figure 1 continued

mean fluorescence intensity and the Spatial Clustering Index, SCI ($n = 3$, quantification made on a representative experiment, at least 38 cells per condition). (**C**) Surface view confocal images showing the effect of Fenpropimorph (Fen) on PM patterning of YFP- St REM1.3 domains 20 hr after agroinfiltration. Tukey boxplots show the mean fluorescence intensity and the SCI of YFP- St REM1.3 in the Mock (DMSO) or Fen-treated leaves ($50 \mu\text{g} / \text{mL}$), at least 46 cells from three independent experiments. (**D**) Secant view confocal fluorescence microscopy images displaying the degree of order of CFP- StREM1.3 - enriched domains (left panel) by the environment - sensitive probe Di - 4 - ANEPPDHQ (middle panel) 48 hr after agroinfiltration. Di - 4 - ANEPPDHQ red / green ratio (RGM) was measured for the global PM, and for the 10, 5, 2 % most intense CFP- St REM1.3 signal-associated pixels (right panel). A lower red / green ratio is associated with an increase in the global level of membrane order, at least 70 cells from three independent experiments. (**E**) Surface view confocal images showing the effect of dead or active constructs of MAP-SAC1p (MAP-mTurquoise2-SAC1p from yeast, see **Figure 1—figure supplement 5**) on PM domain localization of YFP- St REM1.3 20 hr after agroinfiltration. Tukey boxplots show the mean fluorescence intensity and the SCI of YFP- St REM1.3, at least 52 cells from four independent experiments. (**F**) Model showing the PI4P-driven targeting of the trimer of St REM1.3 to the PM and its PI4P- and sterol-dependent nanodomains organization. In all panels, p - values were determined by a two-tailed Mann-Whitney test.

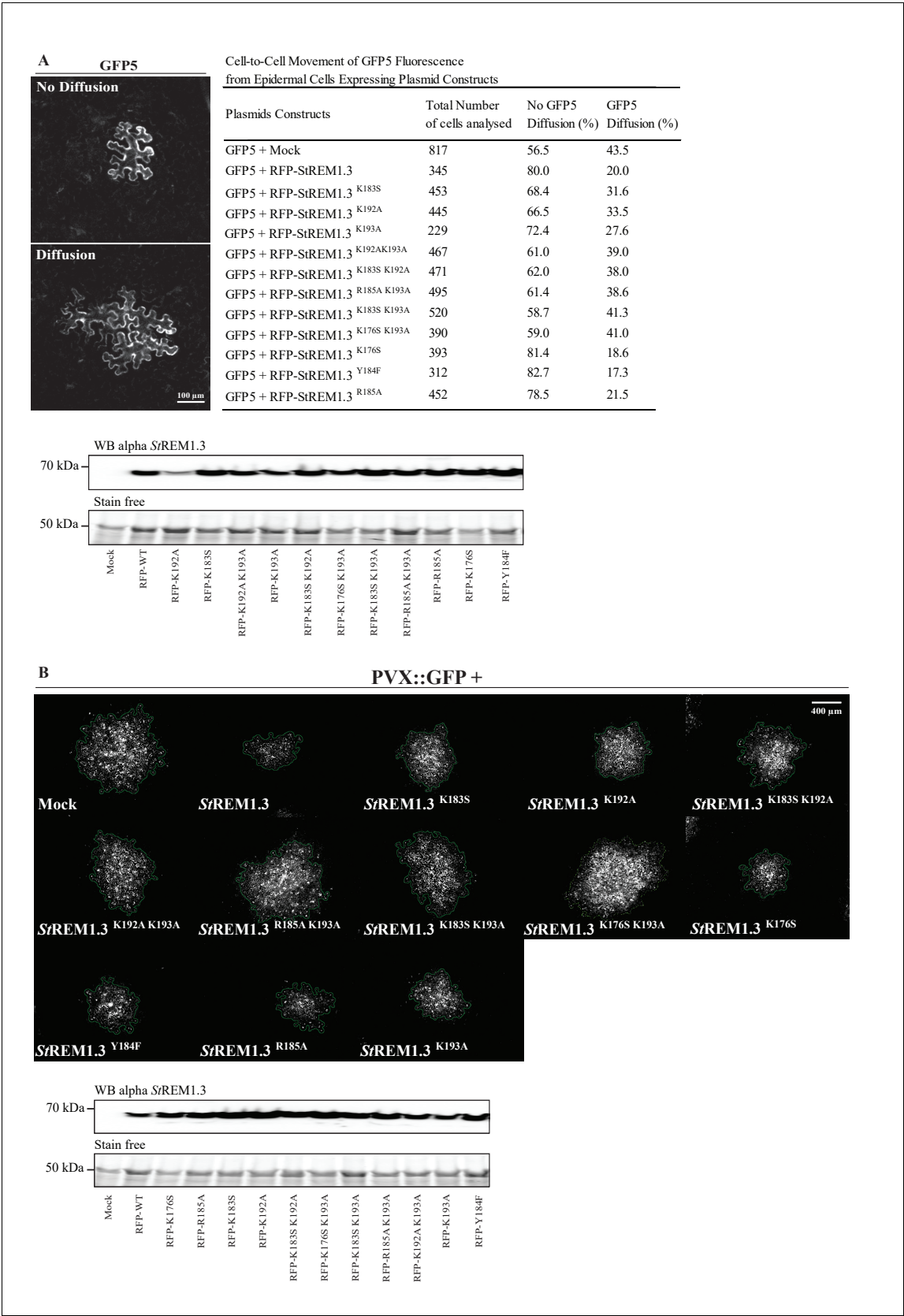


Figure 1—figure supplement 1. Sequence alignment of 51 group 1 REMORIN C-terminal Anchor sequences.

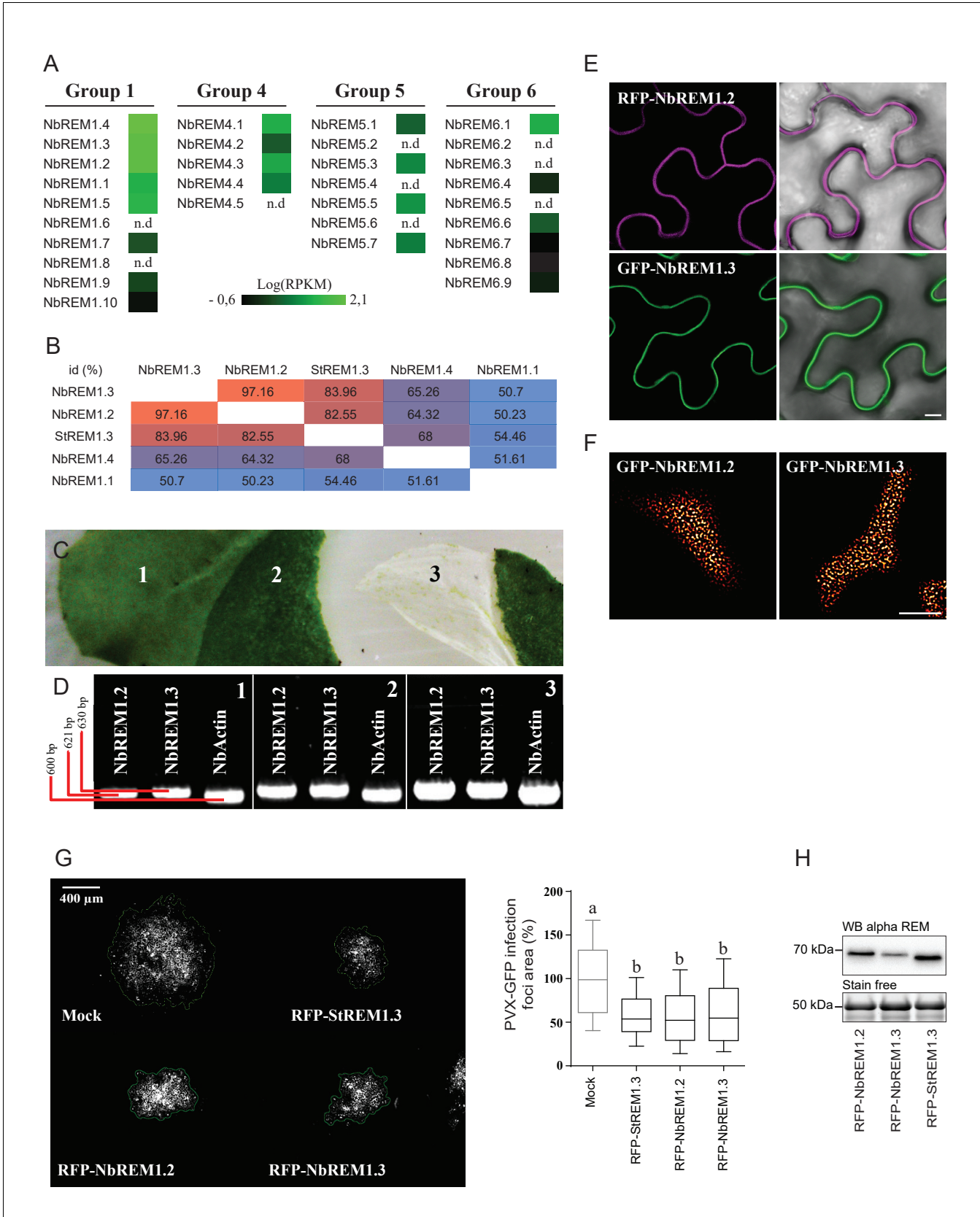


Figure 1—figure supplement 2 continued

Kilobase of transcripts per million mapped reads (RPKM). RNAseq data were retrieved using SRA toolkit (see experimental section). (**B**) Pairwise comparison of protein identity for St REM1.3 and closest group 1 Nb REMs expressed as a percentage of identity. (**C**) Photo of epidermis peeling performed on a glass slide freezing with liquid nitrogen to reduce transcriptional modification due to mechanical stress. Leaf tissue (1) without skin (2) and epidermis (3). (**D**) The expression of endogenous Nb REM1.3 and NbREM1.2 in epidermis was revealed by RT-PCR. (**E, F**) Confocal microscopy pictures of transiently expressed RFP- Nb REM1.2 and GFP- Nb REM1.3 transiently-expressed via *A. tumefaciens* in *N. benthamiana* epidermal cells at 2 DAI show that they both localize in PM-nanodomains. Scale bar indicate 10 μm . (**G**) Propagation of PVX :: GFP alone and in combination with *A. tumefaciens* carrying empty vector (mock), RFP- St REM1.3, RFP- Nb REM1.2 or RFP- Nb REM1.3, and corresponding quantification. Scale bar indicate 400 μm . $n = 4$. Letters indicate significant differences revealed by Tukey's comparisons test $p < 0.001$. (**H**) Total proteins extracted from leaf samples and probed by anti-StREM1.3 antibodies.

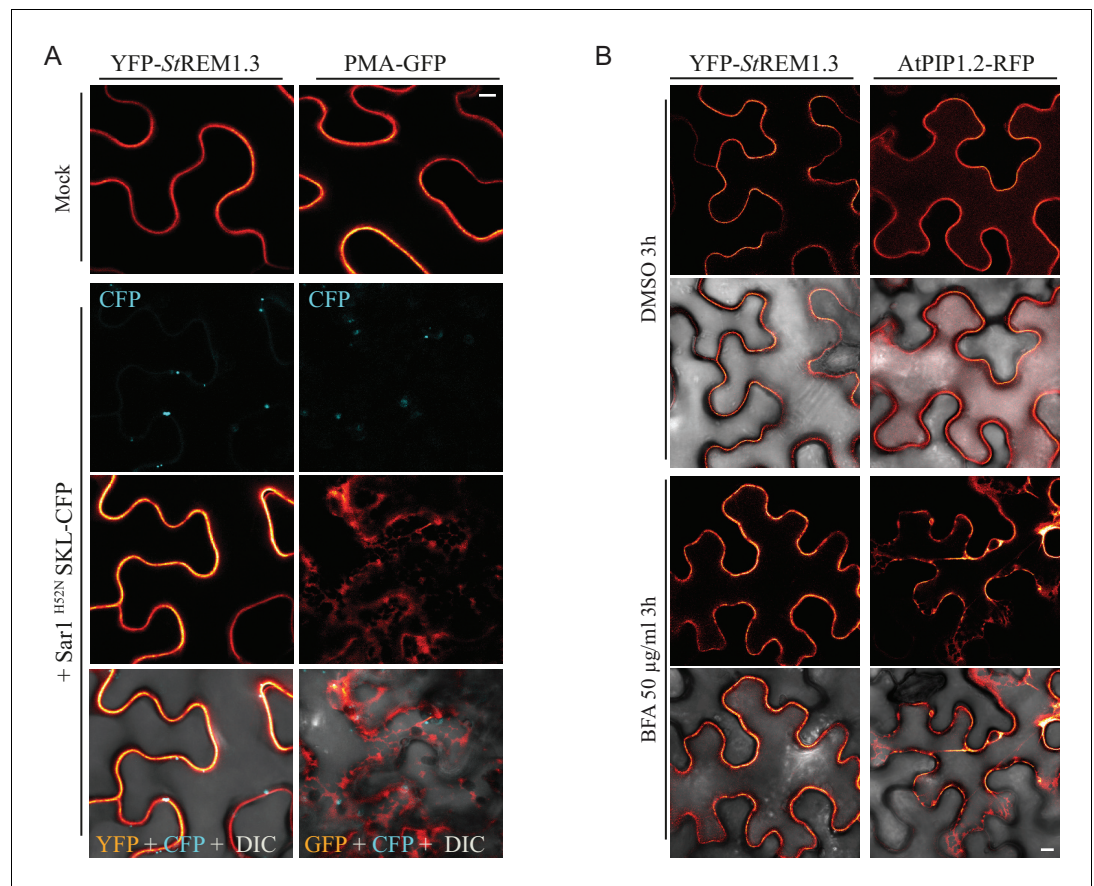


Figure 1—figure supplement 3. YFP- St REM1.3 is targeted to the PM-domains by a mechanism independent of the COP-I / COP-II secretory pathway. (**A**) Secant view of confocal dual-color imaging of *N. benthamiana* expressing YFP- St REM1.3 or proton pump PMA4-GFP (used as positive control) with or without dominant-negative Sar1^{H52N} / SKL-CFP 24 hr after agro -infiltration, SKL-CFP is used as a transformation control (**de Marcos Lousa et al., 2016**). DIC: differential interface contrast. Scale: 10 µm . Lower pictures show merged images. (**B**) Secant view of confocal images of *N. benthamiana* expressing YFP- St REM1.3 or aquaporin At PIP1.1-RFP with or without Brefeldin A, 48 hr after agroinfiltration. Scale bar: 10 µm .

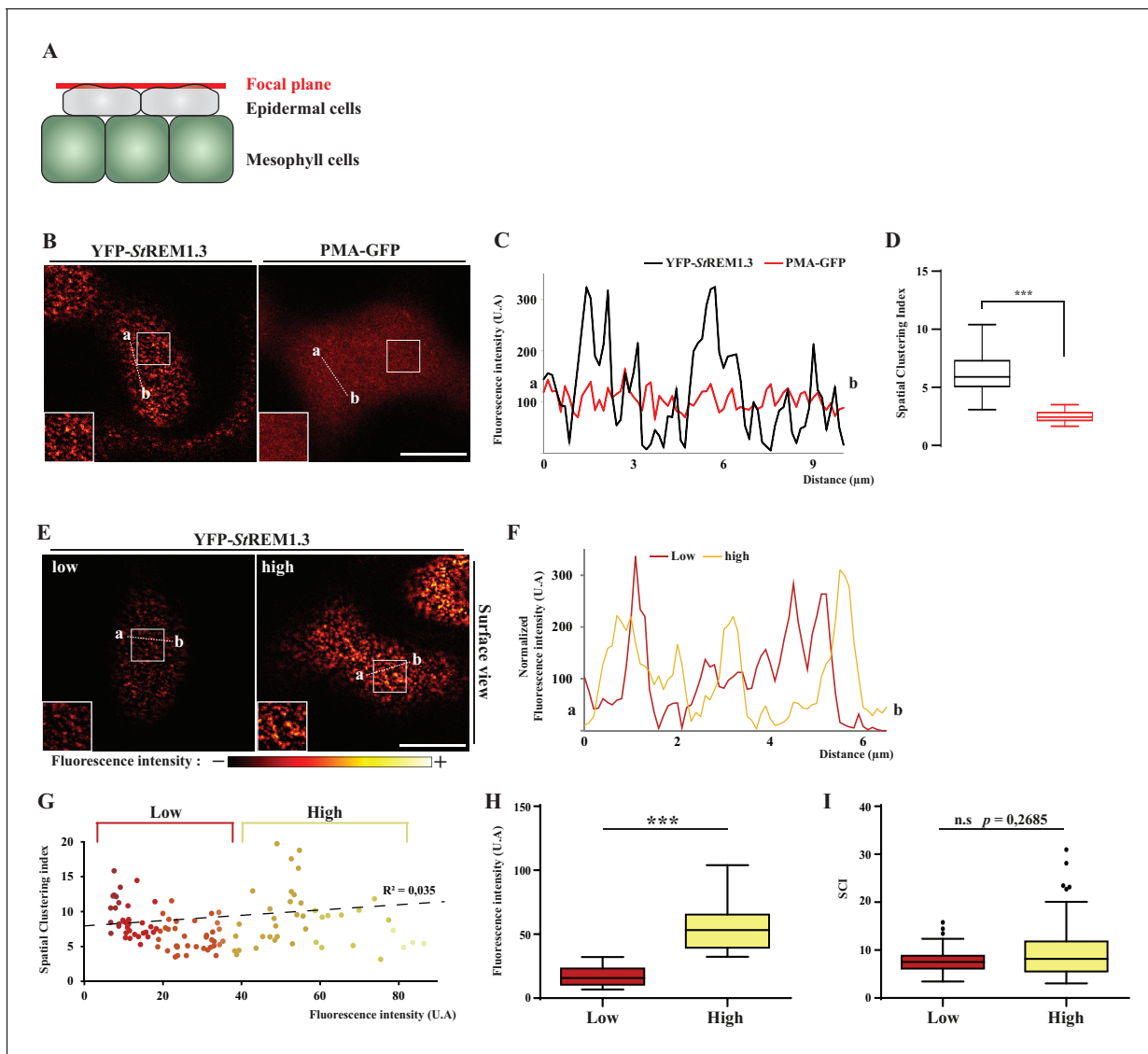


Figure 1—figure supplement 4. Spatial clustering index calculated as the max-to-min ratio of fluorescence intensity in the PM. (A, B). Surface view confocal images of *N. benthamiana* epidermal cells expressing YFP- *StREM1.3* or PMA4-GFP 48 hr after agroinfiltration. (C) Fluorescence Intensity plots through the indicated lines. (D) Spatial Clustering Index (SCI) was calculated by dividing the mean of the 5 % highest values by the mean of 5 % lowest fluorescence intensities values (UA) in the PM. Comparison of SCI show the difference of clustering between PMA4 (smooth location, n = 27 cells) and *StREM1.3* (discrete location, n = 22 cells), significance tested by a two-tailed Mann-Whitney test. E, FG) SCI is not correlated with fluorescence intensity. Surface view confocal images and intensity plots along the indicated lines of *N. benthamiana* epidermal cells expressing low or high levels of YFP- *StREM1.3*. (H) Tukey boxplot showing statistical differences in fluorescence intensity of cells expressing low or high levels of YFP- *StREM1.3*, n = 17. (I) SCI calculated for cells expressing low or high fluorescence levels of YFP- *StREM1.3* showing no difference in YFP- *StREM1.3*-associated nanodomains in the PM between the two levels of expression. Different italicized-letters indicate significant differences among means (p < 0.001, two-tailed Mann-Whitney test).

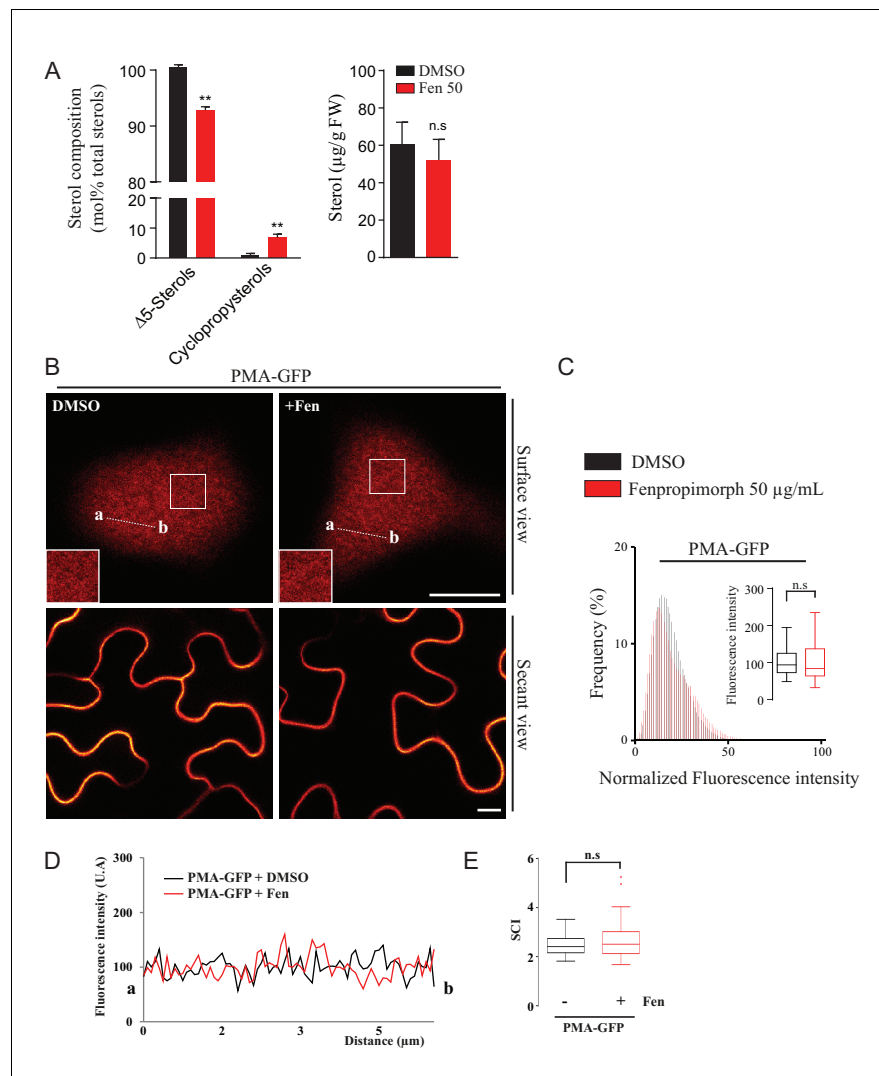


Figure 1—figure supplement 5. Modification of the sterol pool of *N. benthamiana* leaves by the drug Fenpropimorph (fen). (A) Quantification by GC-MS of the $\Delta 5$ phytosterols and cycloartenol from control and fen-treated *N. benthamiana* leaves (n = 3, error bars indicate SEM). Cycloartenol accumulation is similar to what was described in (Grisson et al., 2015). (B) Confocal images of surface or secant views of control and fen-treated *N. benthamiana* leaf epidermal cells expressing PMA4-GFP 48 hr after agroinfiltration. (C – E) Intensity plots and SCI of PMA4-GFP after fen treatment. Scale bars, 10 μm .

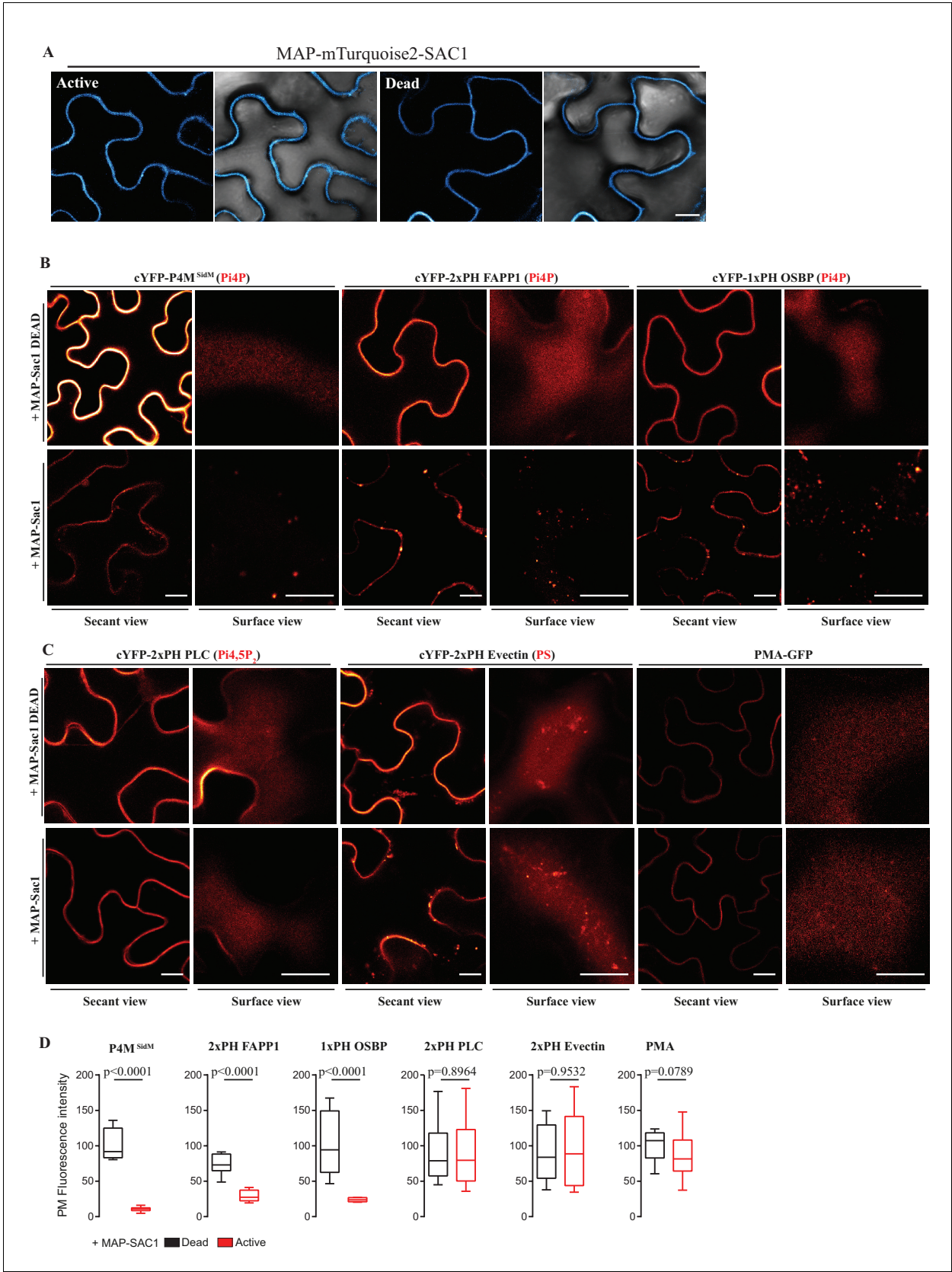


Figure 1—figure supplement 6. Myristoylation and Palmitoylation (MAP) -mTurquoise2-SAC1p localizes at PM of *N. benthamiana* leaf epidermal cells and specifically depletes PM PI4P but not PI (4,5) P₂ or PS. (**A**) Secant view confocal images of *N. benthamiana* leaf epidermal cells expressing either

Figure 1—figure supplement 6 continued on next page

Figure 1—figure supplement 6 continued

Dead or Active MAP-mTURQUOISE2-SAC1p from yeast constructs and P19 to increase expression (**Baulcombe and Molnár, 2004**). Observations were made 48 hr after agroinfiltration. Scale bar, 10 μm . (**B**) Secant view confocal images of *N. benthamiana* leaf epidermal cells expressing three independent PI4P binding domain biosensors: cYFP-P4M^{SidM}, mCitrine-2xPH (FAPP1) and mCitrine-1xPH (OSBP1) (**Simon et al., 2014**) alone or co-expressed with either active or dead MAP-mTurquoise2-SAC1p (**Simon et al., 2016**). (**C**) Secant and surface view confocal images of *N. benthamiana* leaf epidermal cells expressing a sensor for PIP₄,5P₂ (cYFP-2xPH PLC), a sensor for PS (cYFP-2xPH Evecin) and the PM protein (PMA4-GFP) with either active or dead MAP-mTurquoise2-SAC1p. Scale bars for secant and surface views, 10 μm . (**D**) Quantification of PM fluorescence intensity for Pi4P, PS, PI (4,5) P₂ biosensors and PMA4-GFP under co-expression with MAP-SAC1p and MAP-SAC1p dead.

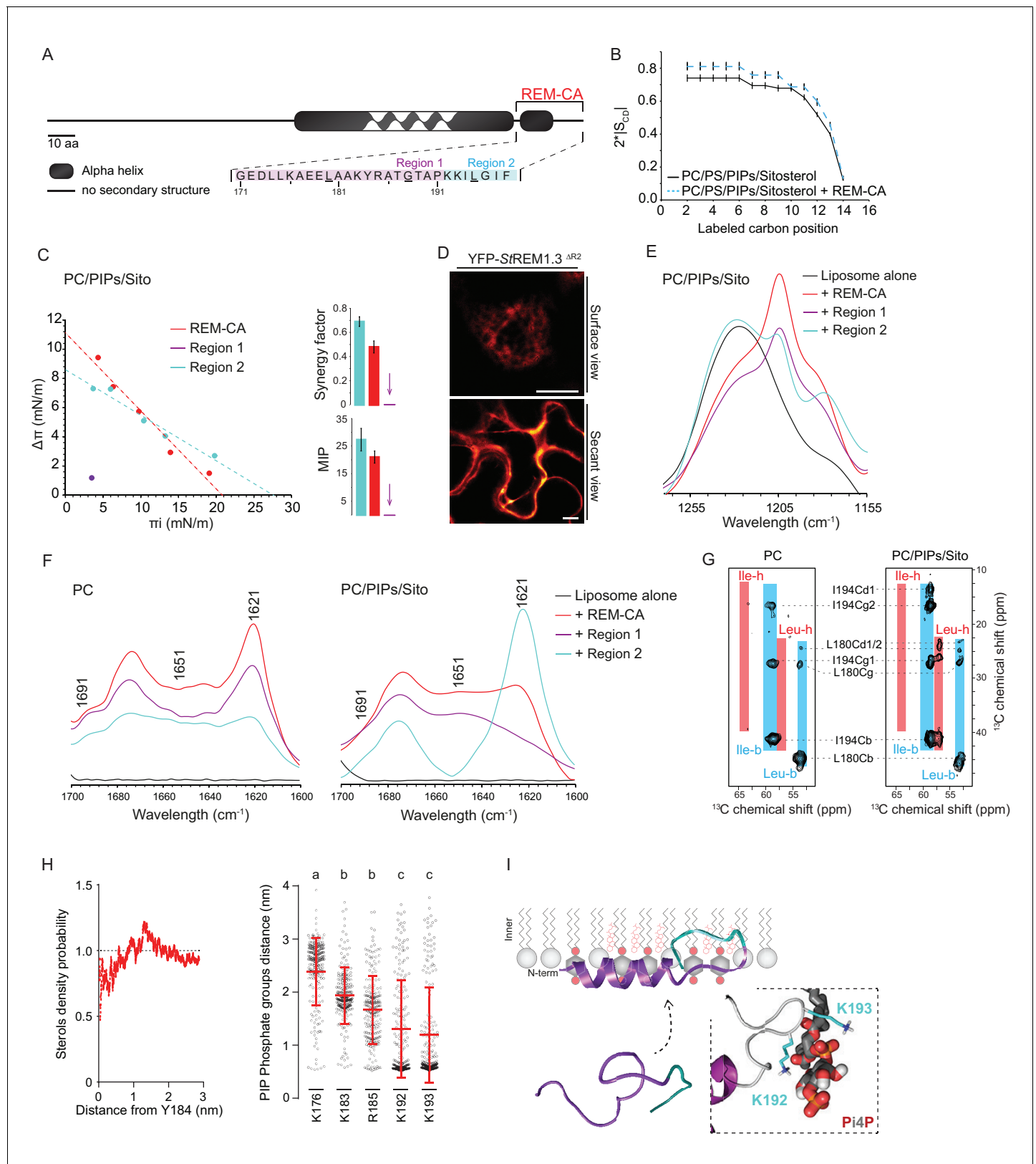


Figure 2. | REMORIN C-terminal anchor peptide is an unconventional PM-binding domain embedded in the bilayer that folds upon specific lipid interaction. (A) Primary sequence of StREM1.3 showing the two putative regions 1 and 2 (R1 and R2) composing the REM-CA. Hatched domain represents the putative coiled-coil helix. (B) Order parameter of the carbon atoms of the fatty acid moiety of all-deuterated 1,2-dimyristoyl-D54-*sn*-3-PC/PS/PIPs/Sitosterol + REM-CA. (C) $\Delta\pi$ (mN/m) vs. π (mN/m) for PC/PIPs/Sito. (D) Surface and secant views of YFP-StREM1.3^{ΔR2}. (E) Wavelength (cm⁻¹) vs. Intensity for PC/PIPs/Sito. (F) Wavelength (cm⁻¹) vs. Intensity for PC and PC/PIPs/Sito. (G) ¹³C chemical shift (ppm) vs. Residue for PC and PC/PIPs/Sito. (H) Sterols density probability vs. Distance from Y184 (nm) and PIP Phosphate groups distance (nm) vs. Residue. (I) Schematic diagram of the REM-CA domain embedded in the lipid bilayer.

Figure 2 continued

phosphocholine (DMPC-d54) in PM inner leaflet-mimicking liposomes revealed by deuterium NMR. (C) Plots of the maximal surface pressure variation ($\Delta\Pi$) vs. the initial surface pressure (Π_i) (left panel) and the corresponding maximal insertion pressure (MIP) and synergy factor (right panel) obtained from the adsorption experiments performed viaa Langmuir trough with a monolayer composed of phosphatidylcholine (PC), phosphoinositides (PIPs) and sitosterol (Sito) (see **Figure 2—figure supplement 3A**). The insignificant $\Delta\Pi$ obtained for D1 indicates that D1 cannot penetrate into the monolayer. (D) Subcellular localization of YFP-StREM1.3 deleted for R2, transiently expressed in *N. benthamiana* leaf epidermal cells. Scale bars, 10 μm . (E) FT-IR spectra measured in the 1155–1255 cm^{-1} absorbance region for the REM-CA, R1 and R2 peptides inserted into MLVs composed of PC:PIPs:Sito (see **Figure 2—figure supplement 3B**). (F) FT-IR spectra in the 1600–1700 cm^{-1} absorbance region for the REM-CA, R1, R2 peptides and liposome alone with MLVs composed of PC alone and PC:PIPs:Sito (see **Figure 2—figure supplement 3B**). (G) Solid-state NMR spectra of REM-CA peptides co-solubilized with DMPC-d54 supplemented with PIPs and Sitosterol (see **Figure 2—figure supplement 3C**). Excerpts on the position of the $\text{C}\alpha$ resonance frequencies of Leucines and Isoleucines on the abscissa are depicted. (H) Radial distribution functions (RDF) of Y184 and sterols, and average distances between the five lysine(K)/arginine(R) residues of REM-CA and the phosphate groups of PI4P during MD simulation, bar indicates mean \pm s.d., letters indicate significant differences revealed by Dunn's multiple comparisons test $p < 0.0001$. (I) Model of the insertion of REM-CA in the PM inner-leaflet based on tensiometry, FTIR, MD and NMR studies. Inset displays Molecular Dynamics (MD) model of the two lysines, K192 and K193, likely in interaction with the phosphate groups of PIPs.

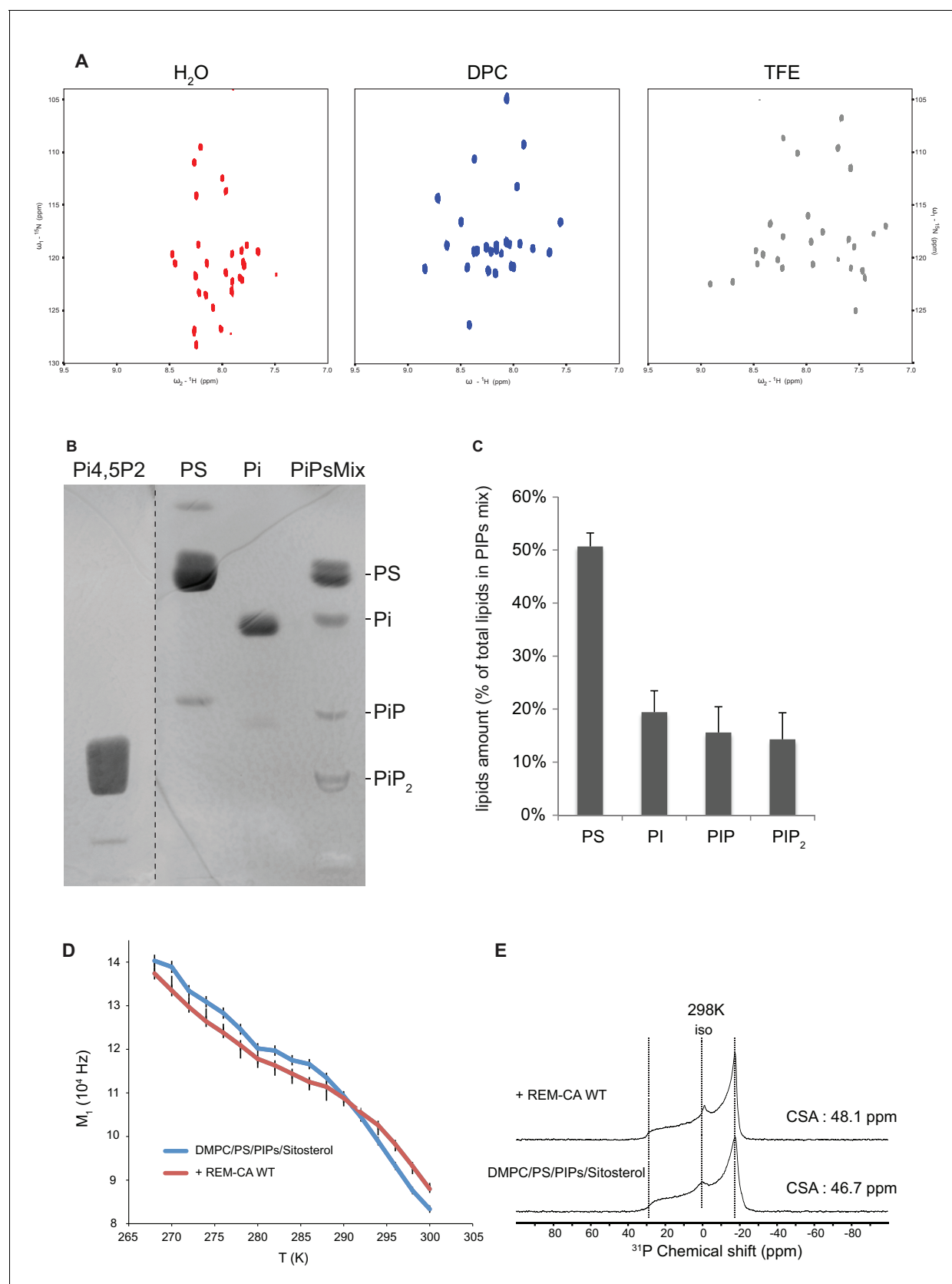


Figure 2—figure supplement 1. Solution NMR and ^{31}P and ^2H solid-state NMR analysis. Thin-layer chromatography analysis of Phosphoinositides mix (PIPs). (A) REM-CA folds in alpha helix in hydrophobic environment. 2D ^1H - ^{15}N correlation spectra of REM-CA recorded at 800 MHz using the SOFAST-PMAG experiment. Figure 2—figure supplement 1 continued on next page

Figure 2—figure supplement 1 continued

HMQC pulse sequence. All spectra were recorded at 25°C with 1 mM of REMCA-WT in H₂O/D₂O (90/10) (red), Dodecylphosphocholine-d38, DPC (blue) and trifluoroethanol-d₂, TFE (grey). (B) Primulin-stained high-performance thin layer chromatography (HP-TLC) plate of the Phosphoinositides mix (PIPs), reference P6023 SIGMA, along with authentic standards: Phosphatidylserine (PS) Phosphatidylinositol (PI), Phosphatidylinositol-4-phosphate (PI4P) and Phosphatidylinositol-4,5-bisphosphate PI(4,5)P₂. (C) Histogram representation of relative amounts of each lipid species present in the PIPs quantified by densitometry scanning. Bars indicate SEM, n = 3. (D) Temperature effect on REM-CA containing liposomes in the range −8°C to 31°C. Heating curves and corresponding NMR lineshape do not show significant changes. (E) ³¹P NMR spectra of deuterated 1,2-dimyristoyl-d54- sn -3-phosphocholine (DMPC-d54) membrane in the absence or presence of REM-CA.

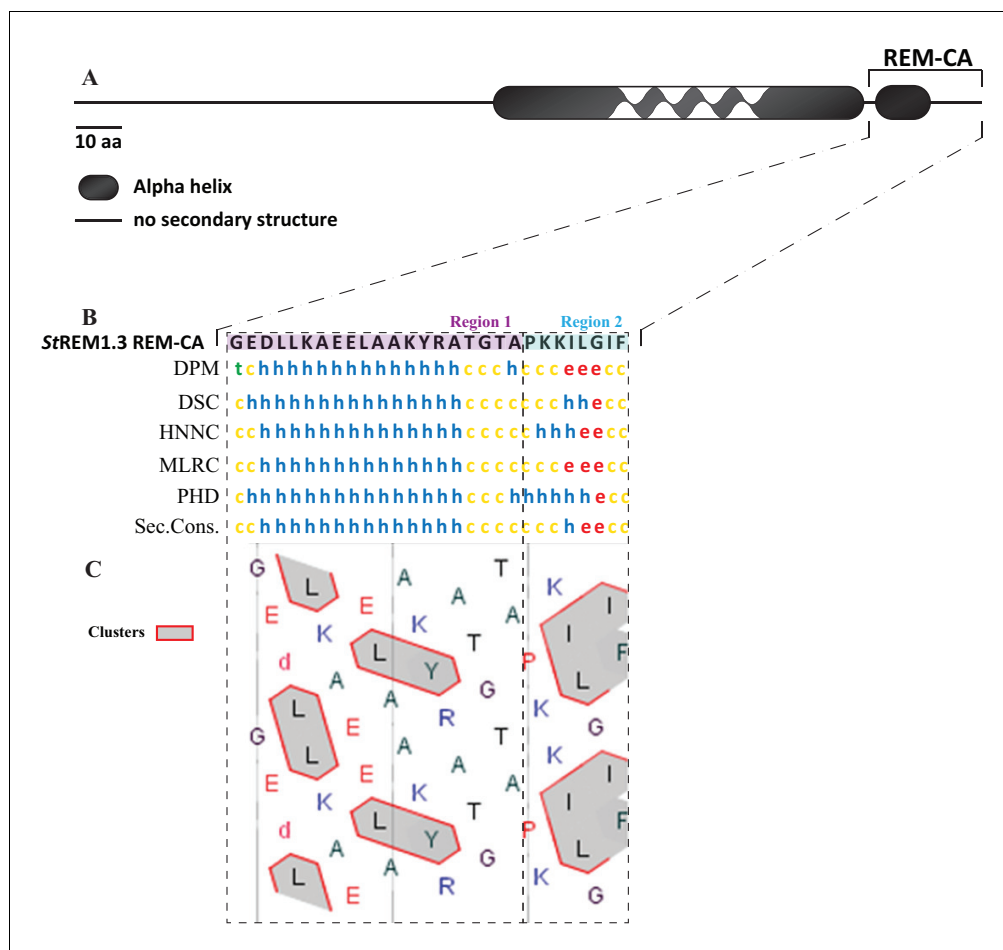


Figure 2—figure supplement 2. In silico analysis of REM-CA from St REM1.3 suggests the existence of two distinct structural regions. (A) Primary sequence of St REM1.3. (B) Sequence and predicted structure of the St REM1.3 REM-CA peptide predicted by different methods, the consensus secondary structure prediction is indicated below; alpha helix (h), random coil (c), beta sheet (e). (C) HCA (hydrophobic cluster analysis) plot of the REM-CA sequence of St REM1.3. V, F, W, Y, M, L and I are hydrophobic residues. These amino acids are circled and hatched to form hydrophobic clusters, see online methods.

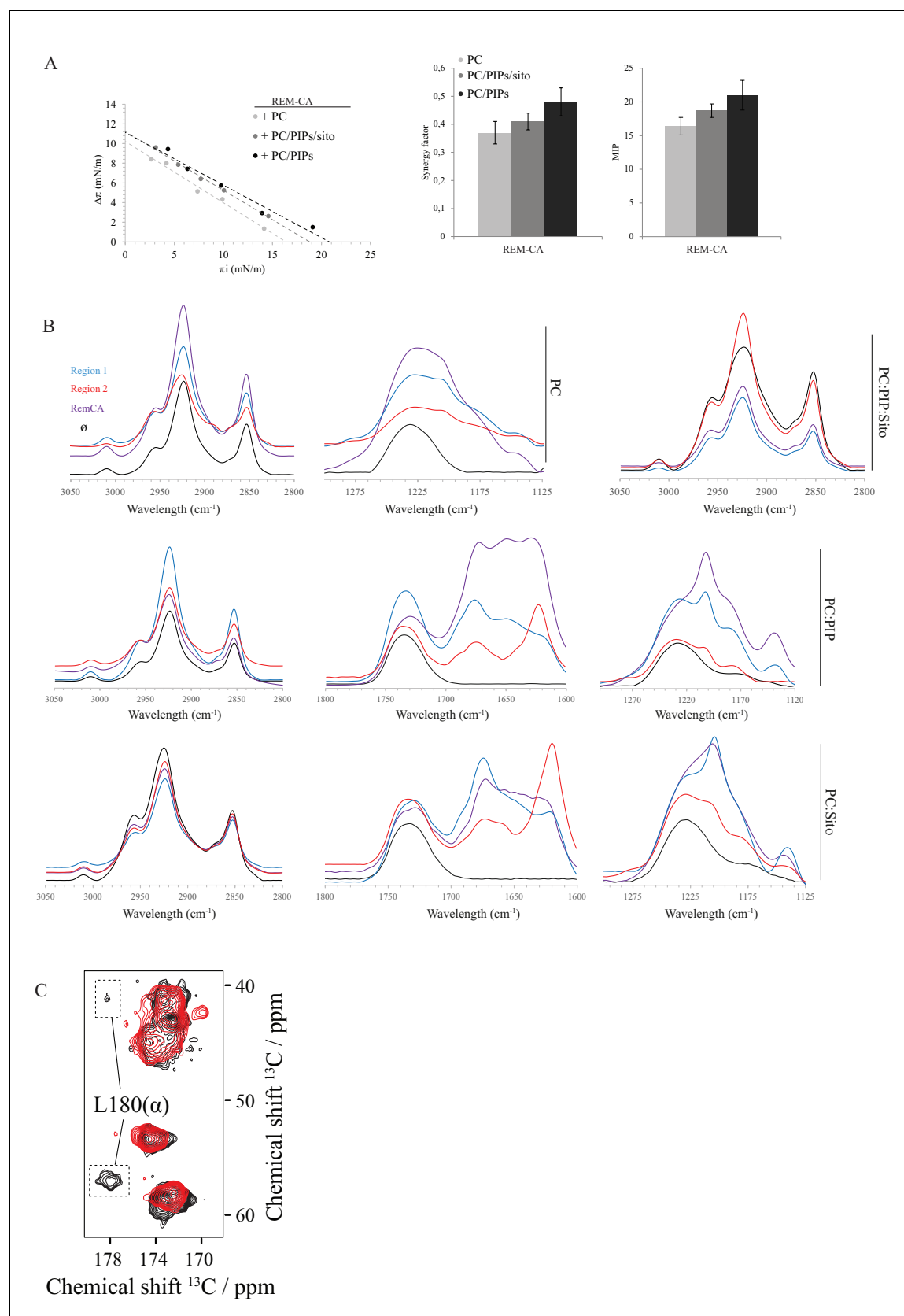


Figure 2—figure supplement 3. Biophysical studies evidence of the interaction of REM-CA with lipids. **(A)** Plots of the maximal surface pressure variation ($\Delta\pi$) vs. the initial surface pressure (π_i) and of the corresponding maximal insertion pressure (MIP) obtained from the adsorption experiments
 Figure 2—figure supplement 3 continued on next page

Figure 2—figure supplement 3 continued

with Langmuir through for REM-CA peptide, with different monolayer compositions i.e. PC alone, PC:PIPs (molar ratio 80:20) or PC:PIPs:Sito (molar ratio 70:20:10). (B) Fourier Transformed-InfraRed (FT-IR) spectra of REM-CA, R1 and R2 peptides in presence of different composition of MLV i.e. PLPC alone, PC:PIP (molar ratio 80:20), PC:Sito (molar ratio 90:10) or PC:PIP:Sito (molar ratio 70:20:10). Three regions of interest of the spectra are shown: the 3050–2800 cm^{-1} region corresponds to the absorbance of lipid alkyl chains, the 1295–1125 cm^{-1} region to the lipid phosphate groups and the 1800–1600 cm^{-1} region to the lipid C=O ester and peptide amide groups. (C) Solid-state NMR structure of REM-CA peptides ^{13}C -labeled at the positions L180, G188 and I184. NMR spectra are shown for membranes containing REM-CA peptides, composed of deuterated 1,2-dimyristoyl-D54-sn-3-phosphocholine, (DMPC-d54), supplemented with sitosterol and Phosphoinositides mix (PIPs), see **Figure 2—figure supplement 1B, C** .

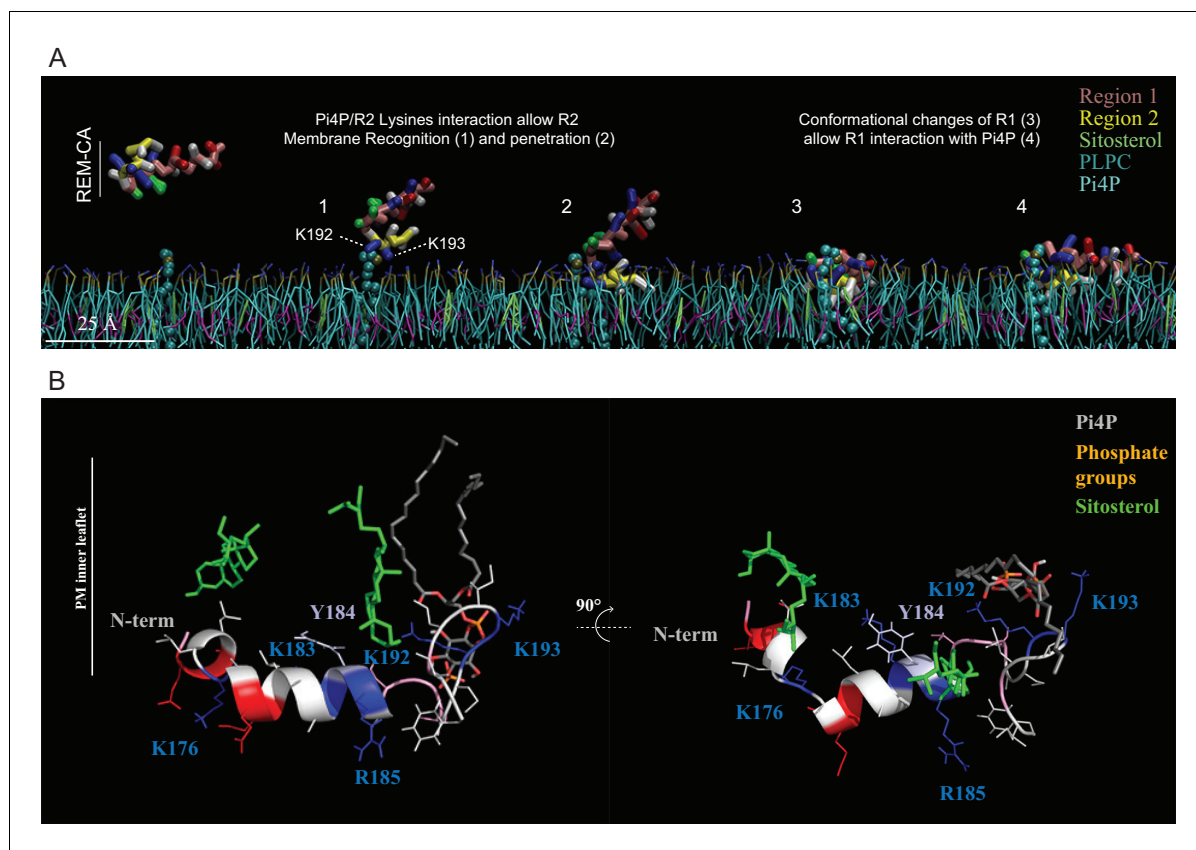


Figure 2—figure supplement 4. Molecular dynamics (MD) simulation reveals interactions between REM-CA residues and lipids in the ternary lipid mixture. (**A**) Snapshots of MD simulations of REM-CA in the presence of a bilayer composed of 1-palmitoyl-2-linoleyl- *sn* -glycerol-3-phosphocholine (PLPC), sitosterol and Pi4P (also see **Video 1**). (**B**) Atomistic structure of REM-CA in PLPC / Pi4P / sitosterol matrix. MD atomistic simulations proposes a model of the inserted structure of REM-CA in the lipid bilayer where peptide-lipid interaction would be mediated by the interaction of REM-CA with the phosphate groups of phosphoinositides and where the lateral ring of tyrosine 184 (Y184) is observed the inside of the membrane.

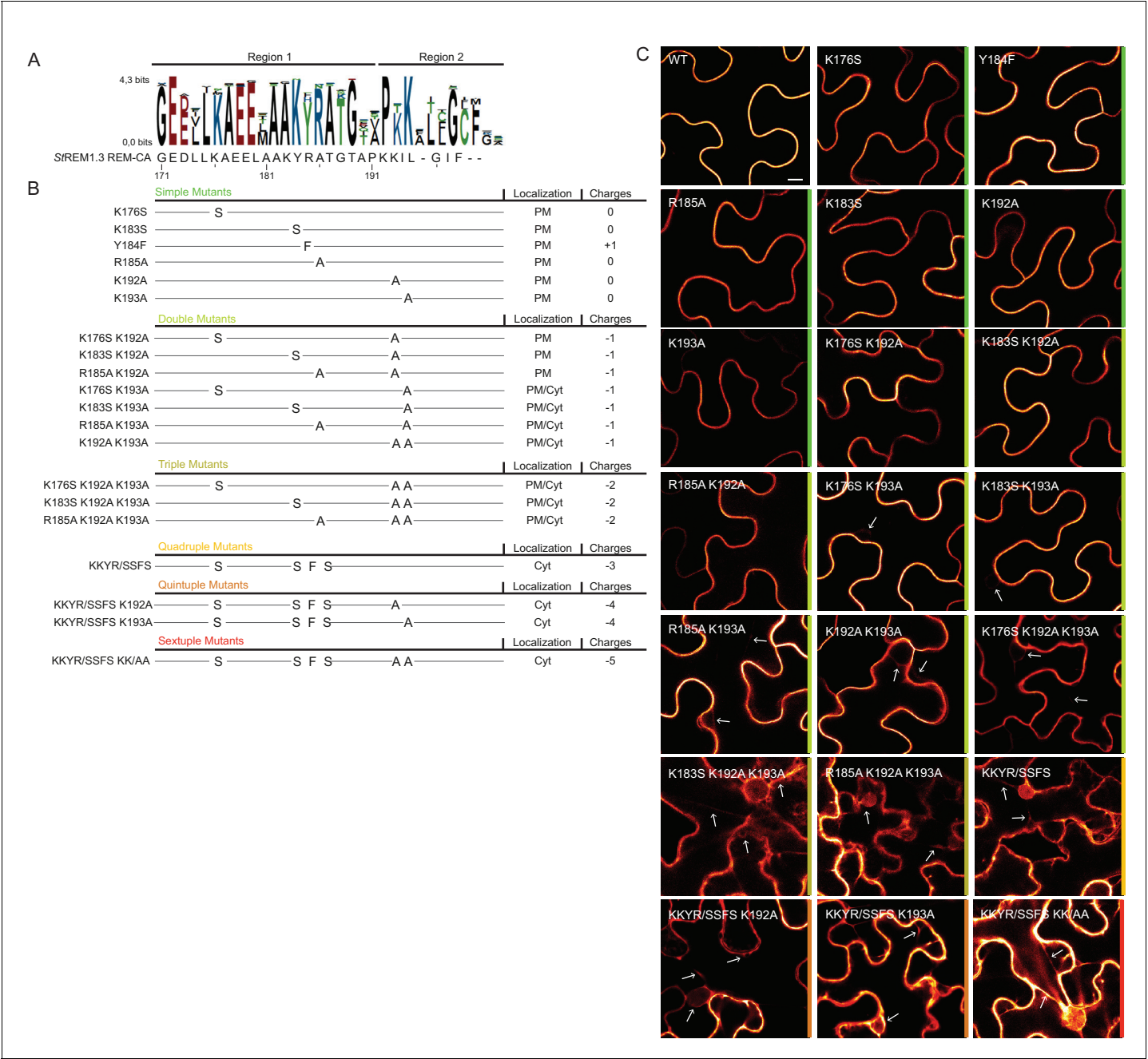


Figure 3. Positively charged residues of REMORIN C-terminal anchor are essential for PM targeting. (A) Sequence Logo obtained from 51 Group 1 REM-CA sequences presented in **Figure 1—figure supplement 1**, and StREM1.3 REM-CA sequence. (B) Summary of the 20 REM-CA mutants of StREM1.3 generated in this study and their corresponding subcellular localizations. PM, Plasma Membrane; Cyt, Cytosol. The total electrostatic charge of each mutated REM-CA is indicated. (C) Confocal images presenting secant views of *N. benthamiana* epidermal cells expressing 20 YFP-StREM1.3 REM-CA mutants (single to sextuple mutations), 48 hr after agroinfiltration. Scale bar of 10µm applies to all images.

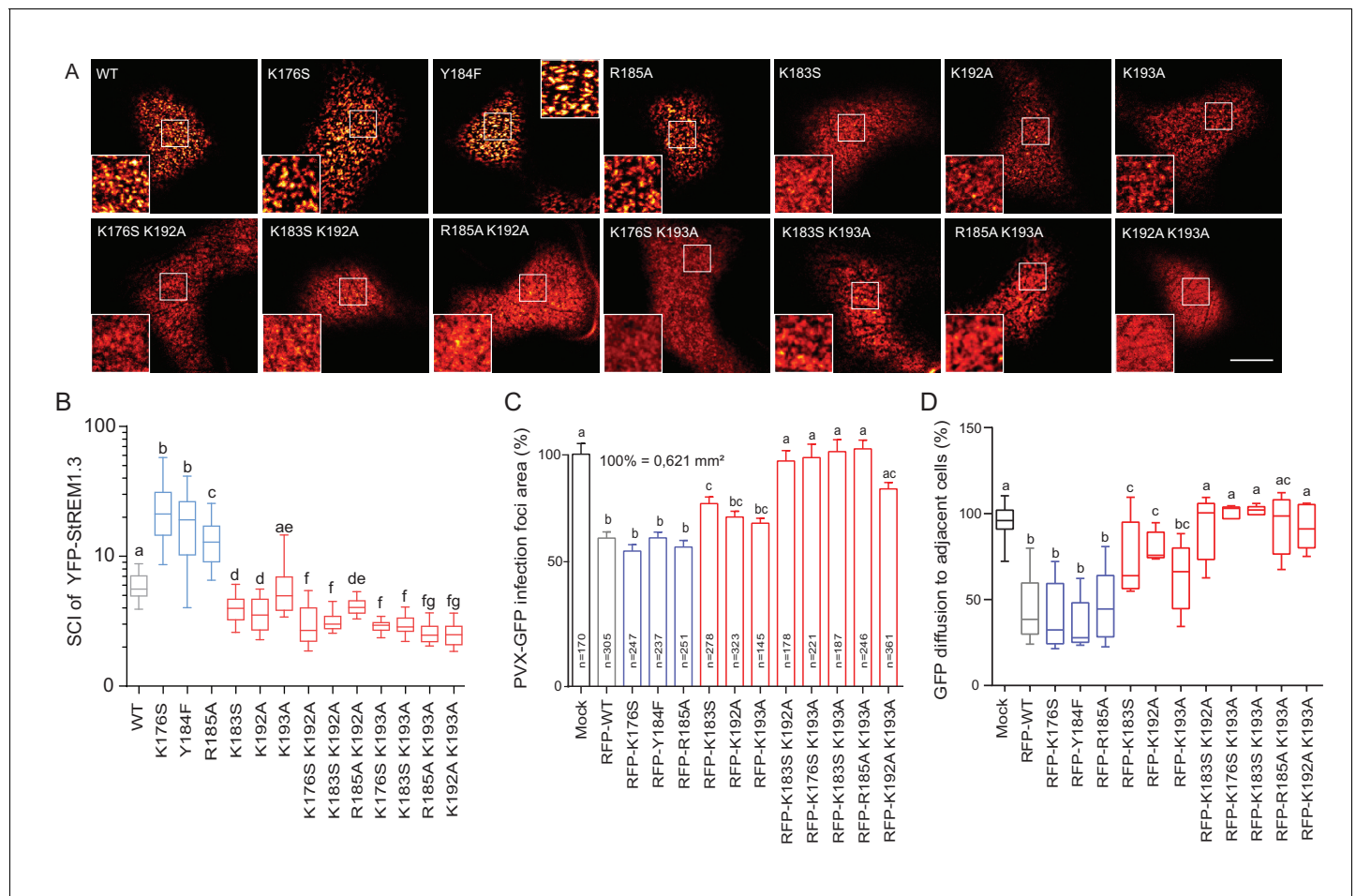


Figure 4. Positively charged residues of REMORIN C-terminal Anchor are essential for PM nanodomain localization and REMORIN function in cell-to-cell permeability. (**A**) Surface view confocal images of the localization of REM-CA single and double mutants. Scale bar, 10 μm . (**B**) Tukey boxplot showing the Spatial Clustering Index of the REM-CA single and double mutants. Letters indicate significant differences revealed by Dunn's multiple comparisons test $p < 0.05$ ($n = 3$). (**C**) Quantification of *Potato Virus X* fused to GFP (PVX: GFP) cell-to-cell movement alone (Mock) or co-expressed with St REM1.3 WT or StREM1.3 REM-CA single and double mutants. Tukey boxplots represent the PVX: GFP infection foci area normalized to the mock condition. Letters indicate significant differences revealed by Dunn's multiple comparisons test $p < 0.05$ ($n = 3$). (**D**) Plasmodesmal permeability assessed in the presence of WT, single or double mutants of REM-CA, according to (*Perraki et al., 2012*). Tukey boxplots represent the percentage of cells presenting a free diffusion of the GFP ($n = 3$), letter indicate significant differences revealed by Dunn's multiple comparisons test $p < 0.05$ (Statistical analysis in *Figure 4—figure supplement 1*).

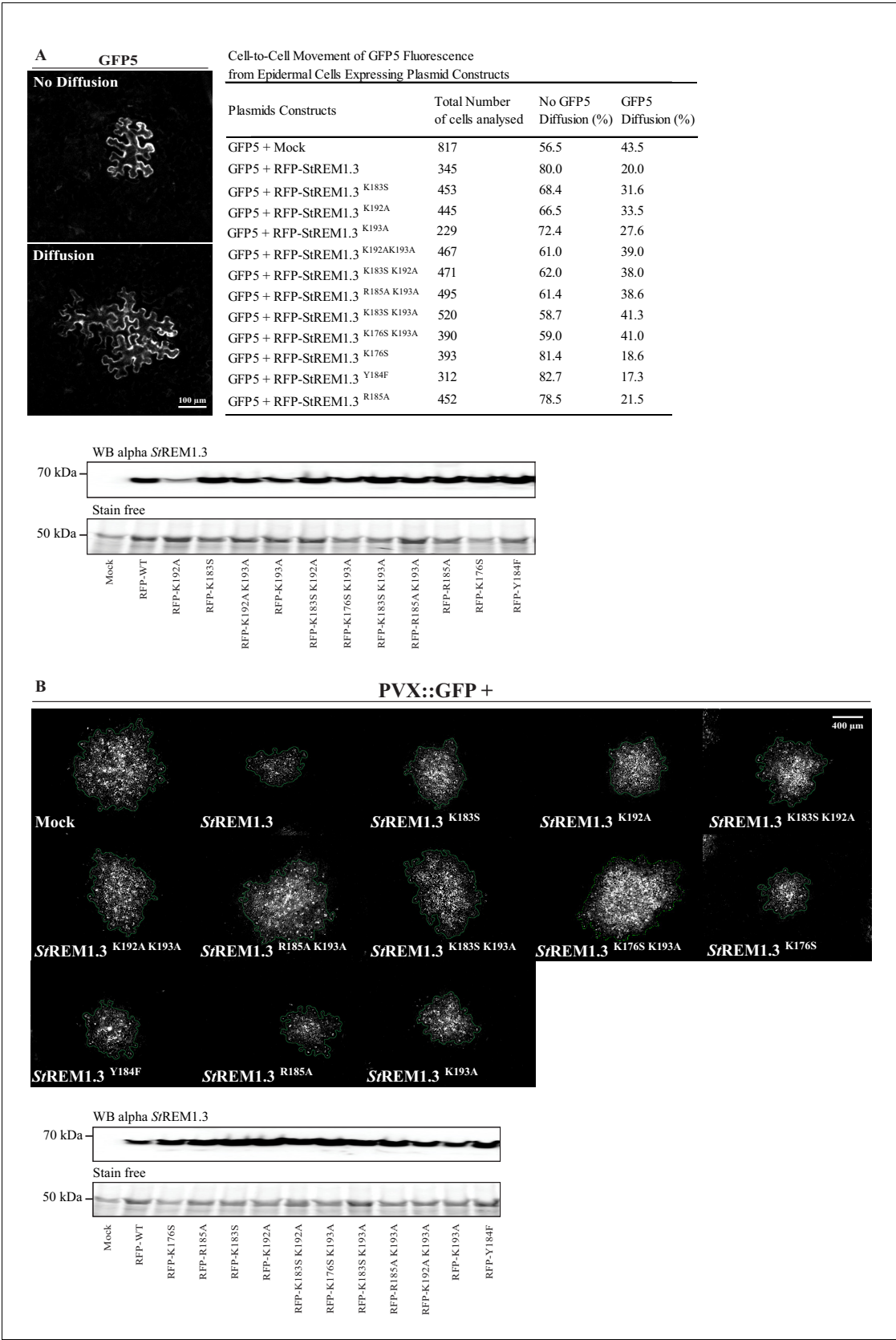


Figure 4—figure supplement 1. Effect of St REM1.3 REM-CA mutant over-expression on plasmodesmata permeability and PVX cell-to-cell movement. (A) Plasmodesmata permeability test performed by visualizing cell-to-cell movement of GFP from a single-cell to its neighbors. Epifluorescence

Figure 4—figure supplement 1 continued on next page

Figure 4—figure supplement 1 continued

microscopy images represent a single-cell where GFP has not diffused to neighboring cells (no Diffusion) and another transformed single-cell where GFP has diffused to three neighboring cells (Diffusion) Scale bar, 100 μm . Plasmodesmal permeability was assessed with GFP alone, or in the presence of RFP- St REM1.3 mutants 5 daysafter infiltration, resume of results obtain from at least three independent experiments are provided in the table. Bottom panel, Total proteins extracted from leaf samples of the plasmodesmal permeability test and probed by anti- St REM1.3 antibodies (**Raffaele et al., 2009**) for each condition. (**B**) Representative epifluorescence microscopy pictures of PVX: GFP infection foci on *N. benthamiana* leaf epidermal cells for 12 RFP- St REM1.3 constructs 5 days after infection. Scale bar, 400 μm . Bottom panel, Total proteins extracted from leaf samples of the PVX: GFP infection assay and probed by anti- StREM1.3 antibodies (**Raffaele et al., 2009**) for each condition.

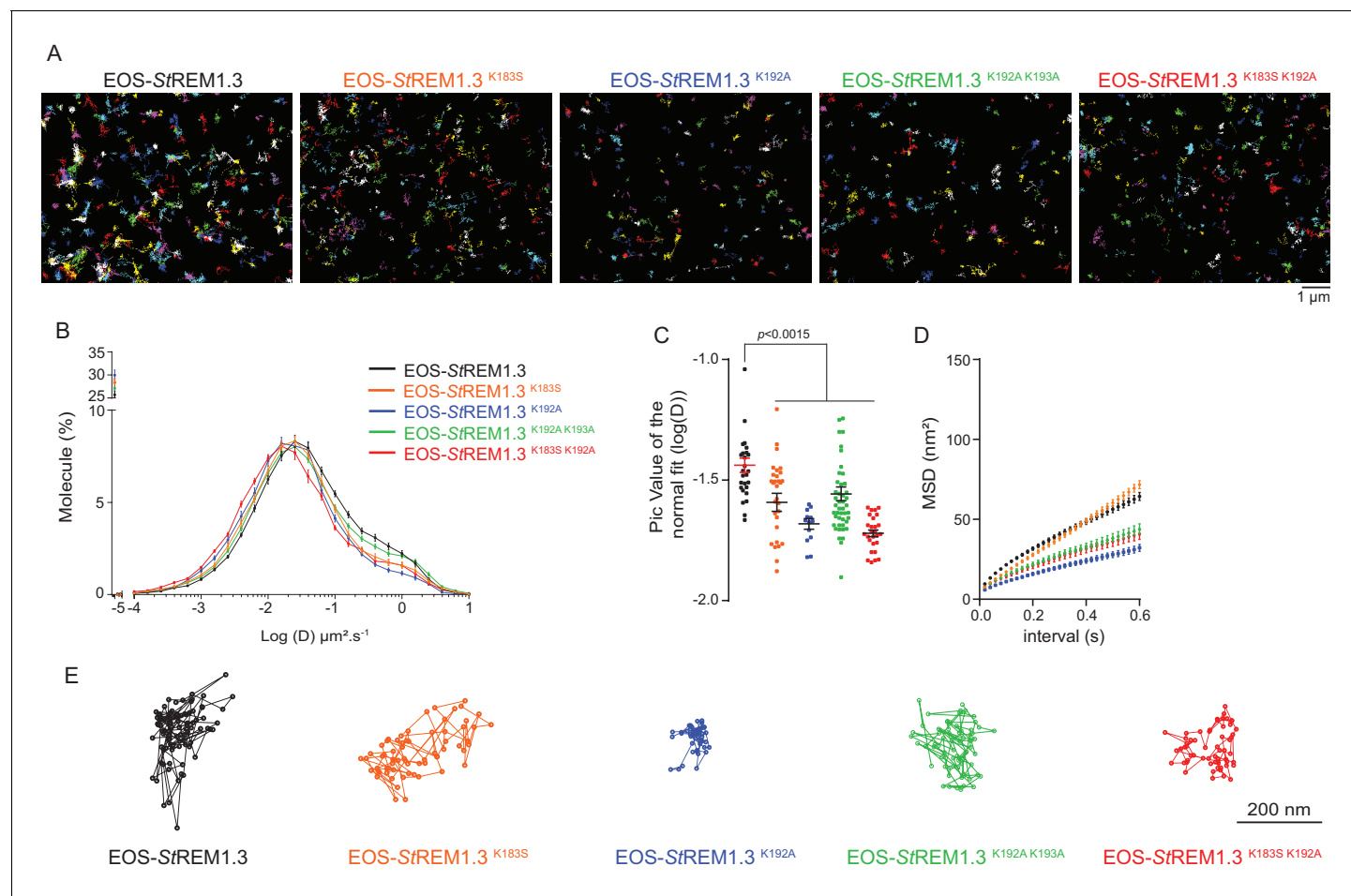


Figure 5. REMORIN C-terminal anchor defines protein mobility in the PM. (A) Super-resolved trajectories (trajectories > 20 points;) of EOS- St REM1.3 WT and REM-CA mutants (K183S, K192A, K183S / K192A and K192A / K193A) visualized by high-resolution microscopy spt-PALM VAEM . 3. (B, C) Distribution of diffusion coefficients (D) represented as log (D) of the different fusion proteins and distributions of the peak D values of individual cells obtained by normal fits and were plotted as log (D), bar indicates mean \pm sem (D) Mean Square Displacement (MSD) over time for the global trajectories > 15 points of each EOS- St REM1.3 construct (n = 13 to 51 cells over three independent experiments). (E) Representative trajectories of St REM1.3 WT and REM-CA mutants. Significant differences revealed by Dunn's multiple comparisons.

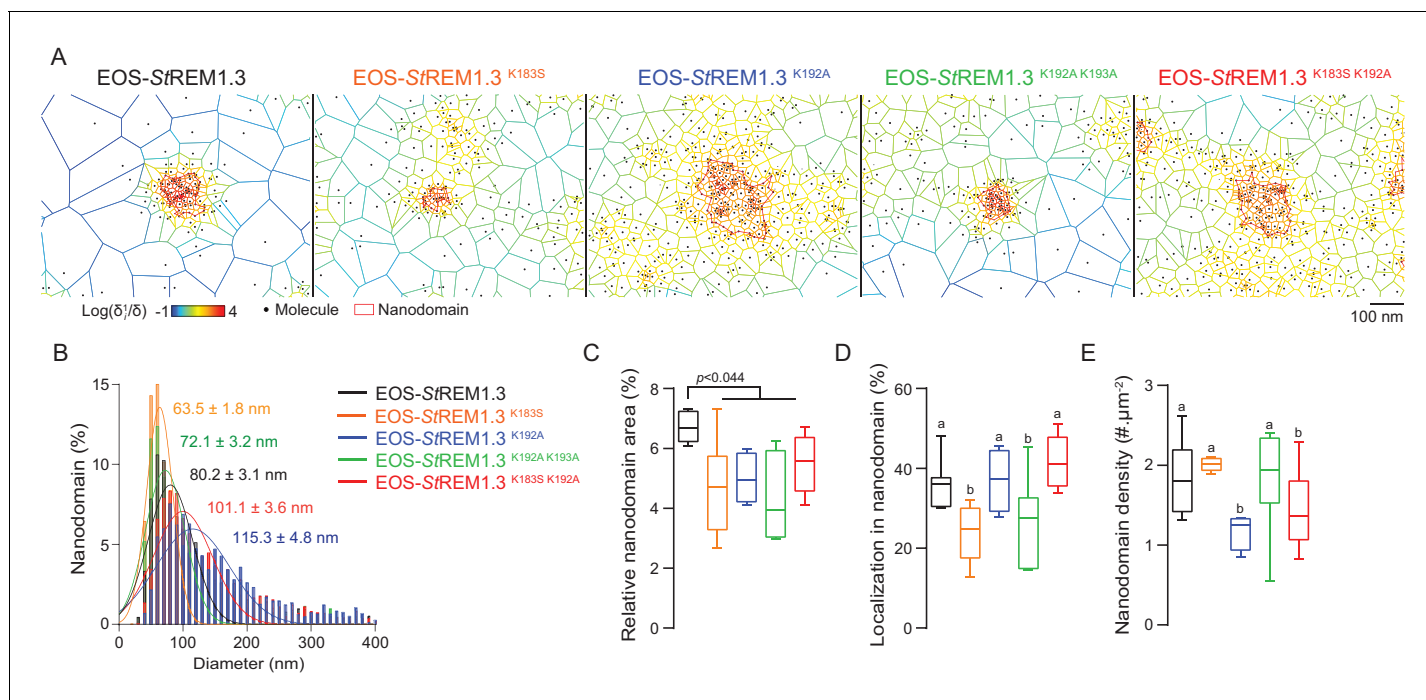


Figure 6. REMORIN C-terminal anchor defines protein segregation in nanodomains. (**A**) Live PALM analysis of molecules localization by tessellation-based automatic segmentation of super-resolution images. (**B**) Diameter distributions of the cluster of EOS fusion proteins (line shows the Gaussian fit). (**C**) Nanodomains surface expressed in percentage of the total PM surface. (**D**) Percentage of molecule localizing in nanodomain. (**E**) Nanodomain density (number of nanodomain.μm⁻²) for the indicated proteins. Statistics were performed on at least six data sets per construction, see online methods for details. Letter indicate significant differences revealed by Dunn's multiple comparisons test $p < 0.05$.